



Anisotropic and hyperelastic identification of *in vitro* human arteries from full-field optical measurements

Stéphane Avril ^{*}, Pierre Badel, Ambroise Duprey

Center for Health Engineering, Ecole Nationale Supérieure des Mines de Saint-Étienne, PECM - CNRS UMR 5146; IFRESIS - INSERM IFR 143, 158 Cours Fauriel, 42023 SAINT-ÉTIENNE cedex 2, France

ARTICLE INFO

Article history:
Accepted 8 July 2010

Keywords:
Vascular mechanics
Identification
Hyperelasticity
Anisotropy
Artery

ABSTRACT

In this paper, we present a new approach for the bi-axial characterization of *in vitro* human arteries and we prove its feasibility on an example. The specificity of the approach is that it can handle heterogeneous strain and stress distributions in arterial segments. From the full-field experimental data obtained in inflation/extension tests, an inverse approach, called the virtual fields method (VFM), is used for deriving the material parameters of the tested arterial segment. The obtained results are promising and the approach can effectively provide relevant values for the anisotropic hyperelastic properties of the tested sample.

© 2010 Elsevier Ltd. All rights reserved.

1. Introduction

It is well assessed that, despite biochemical and hemodynamical factors play a primary role in the development of most vascular disorders, solid mechanics models may contribute to understand their genesis and progression. The realism of models in solid mechanics depends significantly on the mechanical properties used as input parameters. Therefore, characterizing the biomechanical properties of arteries remains an essential issue.

In vivo measurements with ultrasounds or magnetic resonance imaging (MRI) techniques provide relevant information on the vascular behavior (Slager et al., 2000; Masson et al., 2008; Avril et al., 2009) although they are not sufficient for a rigorous determination of arterial wall constitutive equations. To investigate the passive structural response of the arterial tissue, a large variety of *in vitro* experimental protocols are available (Humphrey, 2002).

Among them, inflation/extension of arterial segments are physiologically meaningful tests since the *in vivo* loading conditions may be reproduced and the native geometry is preserved (Hayashi, 1993). Classically, for the analysis, it is assumed that the artery is a perfect cylinder and that the loading induces a homogeneous stress and strain distribution (Humphrey, 2002; Fung, 1993). These assumptions provide a framework for deriving stress–strain curves and to fit them by appropriate constitutive models.

However, inverse approaches should generally be employed since stresses and strains are always heterogeneous, because of

non-cylindrical shape (Holzapfel, 2004; Humphrey, 1999), locally varying material properties or experimental artifacts like edge effects (Arimitsu et al., 1995).

The combination of 3-D deformation measurements (Rastogi, 1999; Foster, 1978; Viotti et al., 2008; Matthys et al., 1991; Genovese, 2007, 2009; Sutton et al., 2007) and inverse approaches (Avril et al., 2008) is now very common in solid mechanics but it is still under-employed for identifying the anisotropic hyperelastic properties of the arterial tissues (Seshaiyer and Humphrey, 2003; Einstein et al., 2005). Moreover, the virtual fields method (Grédiac et al., 2006), which is an inverse method specifically dedicated to full-field data, has never been used for the mechanical identification of arterial tissues although it has very relevant assets: insensitivity to the uncertainty of boundary conditions (Grédiac et al., 2006), robustness (Avril et al., 2004), fast convergence (Avril and Pierron, 2007).

This paper attempts to give a new contribution for addressing the mechanical identification of arterial tissues by presenting an implementation of the virtual fields method to full-field experimental data measured on the whole surface of an arterial segment during inflation/extension tests. The objective of the paper is to present the principle of the approach and to prove its feasibility on an example.

2. Materials and methods

2.1. Materials

Results reported in this paper are obtained on a fairly straight segment of a human ascending aorta (initial length: $L_0 \approx 35$ mm, initial average radius: $R_0 \approx 10$ mm, initial average thickness: $e_0 \approx 1.3$ mm). This vascular segment has

^{*} Corresponding author.

E-mail address: avril@emse.fr (S. Avril).

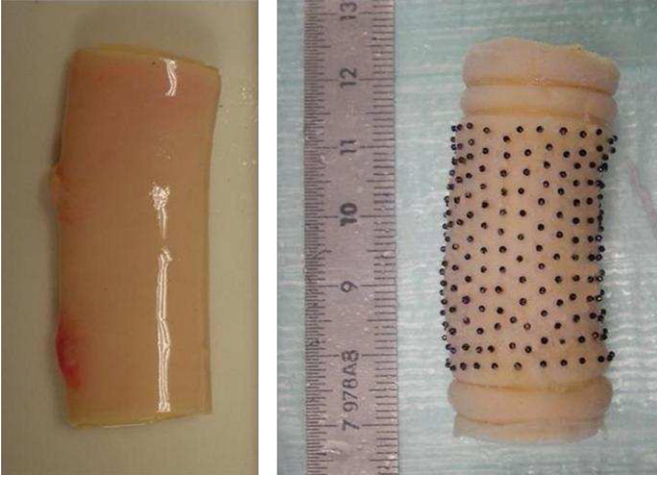


Fig. 1. Picture of the arterial segment used in the tests.

been obtained from a cadaveric 65-year-old female donor. All procedures were carried out in accordance with the guidelines of the Institutional Review Board of the University Hospital Centre of Saint-Etienne, France. After gently cleaning the artery with physiological solution, two side branches were clamped with surgical suture threads (Fig. 1).

2.2. Experiments

This study results from a collaboration between the University of Basilicata (Italy) and Ecole des Mines de Saint-Etienne (France). The experimental setup was developed at the University of Basilicata and presented in a companion paper (Genovese, 2009). The current paper focuses on the inverse approach and all the details about the experimental techniques may be found in Genovese (2009).

The sample was mounted on the *in vitro* rig and preconditioned via eight pressurization cycles from $p=0$ to 80 mmHg (10.5 kPa) and then eight cycles of axial stretching from $L/L_0=1$ to 1.4. Then, different sets of inflation/extension tests were performed.

Let Ψ_t denote the geometrical deformation of the artery induced by the loading at time t , such as $\mathbf{x}(t) = \Psi_t(\mathbf{x}_0)$, where $\mathbf{x}(t)$ is the position vector of a material point at t and \mathbf{x}_0 is the initial position vector of the same material point.

The vascular segment is covered with N ($N \approx 300$) black spherical markers (Fig. 1). The markers were fixed with cyanoacrylate adhesive which was shown not to diffuse in the tissues (Holzapfel et al., 2007). The optical measurement presented in Genovese (2009) provides a point-wise evaluation of Ψ_t at all the points where a marker has been bonded, with an accuracy of 0.17 mm.

During all the inflation/extension tests, the artery remains in a bath of physiological solution. The optical technique was calibrated accounting for the bath of physiological solution around the artery (Genovese, 2009). However, the artery was not hydrated while we bonded the markers. This lasted less than 1 h. This could be reduced in the future by using glue that activates with water.

2.3. Derivation of the field of Green–Lagrange strain tensors

The surface of the artery is meshed for interpolating Ψ_t across the whole artery from the data measured at the marker position. Triangular elements with linear interpolation functions are used. The mesh is defined using a Delaunay triangularization algorithm applied onto the marker initial positions (actually the marker position means the contact position of the marker onto the surface of the artery). Each triangular element is labeled by an index denoted q . Let $\mathbf{x}^q(t)$ denote the position vector of the center of gravity of each element at time t .

Eventually, Ψ_t is known everywhere across the meshed area of the artery. Let Ω be this domain across which the deformation is measured. Ω is defined in the initial configuration because the deformation is Lagrangian. Let $\omega(t)$ be the counterpart of Ω in the deformed configuration at time t .

All the derivations presented in this paper are based on the theory of finite deformations (Ogden, 1997). Let $\mathbf{F}(\mathbf{x}_0, t)$ denote the deformation gradient:

$$\mathbf{F}(\mathbf{x}_0, t) \equiv \nabla \Psi_t(\mathbf{x}_0)$$

where ∇ is the gradient operator.

Then we define the right Cauchy–Green tensor:

$$\mathbf{C}(\mathbf{x}_0, t) \equiv \mathbf{F}^T \mathbf{F}$$

where \mathbf{F}^T is the transpose of \mathbf{F} .

Eventually, we define the Green–Lagrange strain tensor:

$$\mathbf{E}(\mathbf{x}_0, t) \equiv [\mathbf{C} - \mathbf{I}]/2$$

where \mathbf{I} is the identity tensor.

2.4. Constitutive equations

Arteries *in vitro* are usually considered as anisotropic visco-hyperelastic materials. Here, the viscoelastic properties are not considered and only the instantaneous and monotonic response is modeled, after preconditioning. Pseudo-elasticity can therefore be applied (Fung, 1993). Hyperelastic models are considered.

In these models, the Cauchy stress tensor, denoted \mathbf{S} , is deduced from the Green–Lagrange strain tensor such as

$$\mathbf{S} = \mathbf{F} : d\Phi/d\mathbf{E} : \mathbf{F}^T + \lambda \mathbf{I} \quad (1)$$

where Φ is the strain energy function depending only on \mathbf{E} and on material parameters. The term $\lambda \mathbf{I}$ comes from the incompressibility and λ is assessed by writing the plane stress condition ($S_{33}=0$).

Different strain energy functions for the anisotropic hyperelastic behavior of arteries may be found in the literature. Some of them are phenomenological (Fung, 1993; Sun and Sacks, 2005) and others are based on the microstructure (Holzapfel et al., 2000). In this study, we consider three different models:

1. The Delfino model (Holzapfel et al., 2000):

$$\Phi' = \frac{1}{2} \beta' [\exp(\alpha' (I_1 - 3)) - 1] \quad (2)$$

where β' and α' are material parameters and $I_1 = \text{tr}(\mathbf{C})$.

2. The 2-D Fung model (Fung, 1993), which may be written as

$$\Phi = \frac{1}{2} \beta [\exp(\alpha_{11}(E_{11})^2 + \alpha_{22}(E_{22})^2 + \alpha_{12}E_{11}E_{22}) - 1] = \frac{1}{2} \beta [\exp(Q) - 1] \quad (3)$$

where β , α_{11} , α_{22} and α_{12} are material parameters and E_{ij} are the components of the \mathbf{E} matrix in the material coordinate system (indice 1 refers to the circumferential direction and indice 2 refers to the axial direction in the local coordinate system).

3. The Holzapfel model (Holzapfel et al., 2000). This model assigns separate strain energy functions to the media layer and the adventitia layer. The simplest form of the strain energy function may be written as

$$\Phi'' = \frac{c''}{2} (I_1 - 1) + \frac{k''_1}{2k''_2} [\exp(k''_2(I_4 - 1)^2) - 1] + \frac{k''_1}{2k''_2} [\exp(k''_2(I_6 - 1)^2) - 1] \quad (4)$$

where c'' and k''_1 are stress-like material parameters, k''_2 is a dimensionless material parameter; I_4 and I_6 are the squares of the stretch component in the two directions of symmetric tissue fibers. Hence, this model prescribes a fiber orientation angle ϕ for each layer, based usually on analysis of microscopy data. The fiber angles for the specimen used in this work were not known, and so the fiber angles are another material parameter to be determined from the experimental data.

2.5. Inverse approach

The virtual fields method (VFM) is an approach dedicated to the identification of material parameters from full-field measurements (Grédiac et al., 2006; Avril et al., 2004; Avril and Pierron, 2007; Promma et al., 2009). It is based on the weak form of equilibrium equations.

Assuming quasi-static conditions and no body forces, the weak form of equilibrium in the deformed configuration may be written such as

$$-\int_{\omega(t)} \mathbf{S} : \mathbf{E}^* dv + \int_{\partial\omega(t)} \mathbf{t} \cdot \mathbf{u}^* ds = 0 \quad (5)$$

where $\partial\omega(t)$ is the boundary of the volume in the deformed configuration, vector \mathbf{t} denotes the tractions applied onto this boundary (pressure forces and axial load), \mathbf{u}^* is a displacement virtual field which acts as a test function in Eq. (5). \mathbf{E}^* is the strain virtual field deduced from the gradient of \mathbf{u}^* :

$$\mathbf{E}^* = \frac{1}{2} (\nabla \mathbf{u}^* + \nabla^T \mathbf{u}^*) \quad (6)$$

At position \mathbf{x} where a marker is located, \mathbf{u}^{*1} and \mathbf{u}^{*2} take the following values:

$$\begin{cases} \mathbf{u}^{*1} = \sin\left(\frac{\pi(z-z_b)}{z_t-z_b}\right) \mathbf{i} \\ \mathbf{u}^{*2} = \frac{z-z_t}{z_b-z_t} \mathbf{k} \end{cases} \quad (7)$$

where

- vectors \mathbf{i} and \mathbf{k} are, respectively, the radial and longitudinal axes in the global cylindrical coordinate system defined in Fig. 2;
- z is the component of \mathbf{x} along the longitudinal axis: $z = \mathbf{x} \cdot \mathbf{k}$;
- z_b and z_t are defined in Fig. 2.

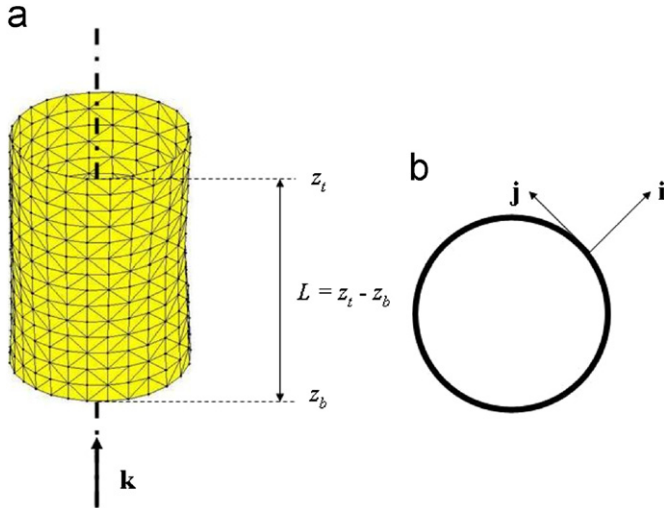


Fig. 2. Meshing and schematic of the initial geometry: (a) 3-D view; (b) cross sectional view.

The rationale behind this choice of virtual displacements is:

- one involves mainly the radial properties (\mathbf{u}^1);
- one involves mainly the axial properties (\mathbf{u}^2);
- both zero the action of unknown reaction forces or involve their resultant if the resultant is measured (Grédiac et al., 2006).

Given the previous points, infinity of virtual deformation may be used. The rationale behind the current choice is that the best results are always obtained with the simplest functions. This was proved in different papers (Grédiac et al., 2006; Avril et al., 2004; Avril and Pierron, 2007; Promma et al., 2009). This can be interpreted like this: a virtual deformation is a test function. If the test function is very smooth, it will average out the randomly distributed errors contained in the experimental data.

Eq. (7) only gives the values of the virtual displacement at marker positions. Between the marker positions, the values of \mathbf{u}^1 and \mathbf{u}^2 are interpolated linearly. Moreover, regarding the external virtual work, it can be written as

$$\begin{aligned} \int_{\partial\Omega(t)} \mathbf{t} \cdot \mathbf{u}^1 ds &= \int_{\partial\Omega(t)} \mathbf{n}_t \cdot \mathbf{u}^1 p(t) ds + \mathcal{F}(t) \mathbf{k} [\mathbf{u}^1(z_t) - \mathbf{u}^1(z_b)] \\ \int_{\partial\Omega(t)} \mathbf{t} \cdot \mathbf{u}^2 ds &= \int_{\partial\Omega(t)} \mathbf{n}_t \cdot \mathbf{u}^2 p(t) ds + \mathcal{F}(t) \mathbf{k} [\mathbf{u}^2(z_t) - \mathbf{u}^2(z_b)] \end{aligned} \quad (8)$$

where \mathbf{n}_t is the unit outer normal vector at t , $\mathcal{F}(t)$ is the axial resultant load measured by a load cell along axis \mathbf{k} . According to the definition of \mathbf{u}^1 and \mathbf{u}^2 in Eq. (7), quantities $[\mathbf{u}^k(z_t) - \mathbf{u}^k(z_b)]$ will be replaced in the following equations by δ_{k2} , where $\delta_{k2} = 0$ if $k=1$ and $\delta_{k2} = 1$ if $k=2$.

As \mathbf{S} is deduced from experimental data, Eq. (5) cannot be satisfied exactly and the principle of the inverse method (Grédiac et al., 2006) is to minimize the squares of residuals, as defined in the following cost function:

$$\begin{aligned} \zeta(\beta, \alpha_{11}, \alpha_{22}, \alpha_{12}) &= \sum_k \sum_m \left[- \int_{\Omega(t_m)} \mathbf{S} : \mathbf{E}^k dv \right. \\ &\quad \left. + p(t_m) \int_{\partial\Omega(t_m)} \mathbf{n}_t \cdot \mathbf{u}^k ds + \delta_{k2} \mathcal{F}(t) \right]^2 \end{aligned} \quad (9)$$

where m labels the time when a measurement is achieved and k labels the virtual field ($k=1,2$).

Considering the interpolation of all quantities with the triangular mesh, the previous integrals in the principle of virtual work may be changed into discrete sums.

$$\begin{aligned} \zeta(\beta, \alpha_{11}, \alpha_{22}, \alpha_{12}) &= \sum_k \sum_m \left[- \sum_q \mathbf{S}(\mathbf{x}^{q,m}) : \mathbf{E}^k(\mathbf{x}^{q,m}) A(\mathbf{x}^{q,m}) e(\mathbf{x}^{q,m}) \right. \\ &\quad \left. + p(t_m) \sum_q \mathbf{n}_t(\mathbf{x}^{q,m}) \cdot \mathbf{u}^k(\mathbf{x}^{q,m}) A(\mathbf{x}^{q,m}) + \delta_{k2} \mathcal{F}(t) \right]^2 \end{aligned} \quad (10)$$

where $A(\mathbf{x}^{q,m})$ denotes the area of triangular element q at time t_m and $e(\mathbf{x}^{q,m})$ denotes the thickness of the artery¹ at \mathbf{x}^q at time t_m . \mathbf{E}^k is derived from the virtual

displacements \mathbf{u}^k using Eq. (6). The virtual displacements \mathbf{u}^k are defined in Eq. (7). The value of p is experimental data and \mathbf{S} is derived using Eq. (1). It must be noted that the model parameters are involved in \mathbf{S} . All the incremental steps are taken into account as the squares of residuals of each incremental step, denoted m , are summed up.

Cost function ζ figures the quadratic gap between the internal virtual work (IVW) and the external virtual work (EVW) where

$$\text{IVW}^{k,m} = e_0 \sum_q \mathbf{S}(\mathbf{x}^{q,m}) : \mathbf{E}^k(\mathbf{x}^{q,m}) A(\mathbf{x}^{q,0})$$

$$\text{EVW}^{k,m} = p(t_m) \sum_q \mathbf{n}_t(\mathbf{x}^{q,m}) \cdot \mathbf{u}^k(\mathbf{x}^{q,m}) A(\mathbf{x}^{q,m}) + \delta_{k2} \mathcal{F}(t) \quad (11)$$

Cost function ζ and IVW are driven by the choice of the unknown material parameters. Eventually, the cost function can be minimized through an iterative scheme using the Nelder–Mead algorithm (Nelder and Mead, 1965). This yields the unknown material parameters.

3. Results

A sample was tested for proving the feasibility of the approach (Figs. 1 and 2). We report data corresponding to eight pressure levels distributed between 0 and 150 mmHg at $L/L_0=1.1$ (Figs. 3 and 4).

The results obtained with the VFM are reported in Table 1 for the Fung model. Convergence of the Nelder–Mead optimization routine was reached in nearly 10 min. The identified values for the Fung material parameters of the artery are consistent with the range orders reported in the literature (Holzapfel et al., 2000; Fung, 1993). Parameter β is usually around 10 kPa. It is interesting to notice the large difference between the value of α_{11} and α_{22} . It means that there is a large anisotropy in this specimen, which has already been reported in the literature (Holzapfel et al., 2000).

It can be observed in Fig. 5 that the gap between the external virtual work and the internal virtual work is very low for the obtained material parameters.

4. Discussion

4.1. Application to the other constitutive models

4.1.1. The Delfino model

The material parameters of Eq. (2), namely α' and β' , can be identified using only \mathbf{u}^1 . This means that only the circumferential response is used for the identification. The results obtained with the VFM for these two material parameters are $\beta' = 1.5$ kPa and $\alpha' = 4.6$.

However, it is interesting to notice in Fig. 6 that the gap between IVW and EVW remains very large for \mathbf{u}^2 when computed with the constitutive equations of Eq. (2) and the material parameters reported above. This indicates irrelevancy of the isotropic assumption. This justifies the choice of anisotropic laws.

4.1.2. The Holzapfel model

Here, having access only to measurements on the surface of the artery, it is only possible to identify the average strain energy function across the whole thickness, but not separately strain energy functions of the media layer and of the adventitia layer. If, as in Marra et al. (2006), the strain energy function is assumed homogeneous across the thickness, then a mean fiber angle and mean values of the other parameters of the Holzapfel model can be identified by the VFM. The obtained results are $c'' = 0.4$ kPa, $k''_1 = 8.7$ kPa, $k''_2 = 5.4$ and $\phi = 27^\circ$. These results show that parameters of a Holzapfel model may be retrieved by the VFM.

Fiber angles and material parameters in human arteries are usually different for the media and the adventitia. Only average

¹ Due to the incompressibility assumption, $A(\mathbf{x}^{q,m}) e(\mathbf{x}^{q,m}) = A(\mathbf{x}^{q,0}) e_0$, with $\mathbf{x}^{q,m} = \mathbf{x}^q(t_m)$.

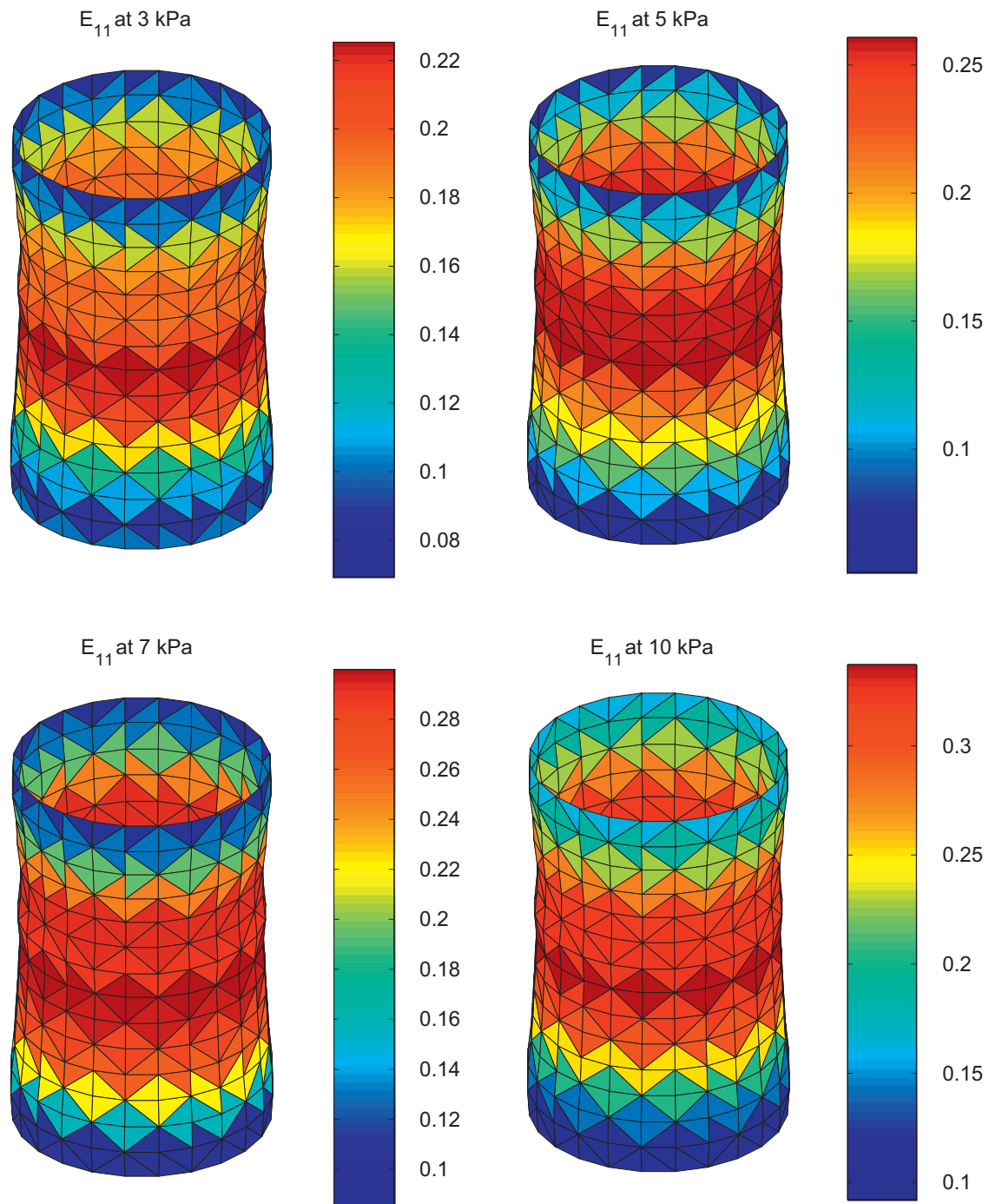


Fig. 3. Plot of the circumferential components of the Green–Lagrange strain tensor for different values of p . The plot is displayed in the undeformed configuration.

values are reported here. A separate identification of media and adventitia constitutive equations would be possible by mechanical separation of the layers of the human artery, as shown in Holzapfel et al. (2000).

4.1.3. Material heterogeneities

Arteries may also have properties varying along the axis. The VFM was already applied successfully to the identification of nonlinear heterogeneous behavior for metals (Sutton et al., 2008). The implementation of a similar approach for arteries is possible but it will require that the spatial resolution is adapted to the length scale of local variations of the material properties. This may be achieved by employing 3-D digital image correlation, as shown in Sutton et al. (2007).

4.2. Discussions for α_{12} in the Fung model

Parameter α_{12} is the coupling factor between E_{11} and E_{22} in the exponential of the strain energy function. It means that α_{12} characterizes the effect of the circumferential strain onto the axial response, or vice versa. A value of 0.1 was found for parameter α_{12} (Table 1). For obtaining this result, the algorithm was initialized according to values² reported in Fung (1993).

However, it must be noted that the results regarding α_{12} are significantly affected by the value input for initializing the optimization algorithm. This may indicate a lack of sensitivity of the

² Initial values: $\beta = 29$ kPa, $\alpha_{11} = 2.5$, $\alpha_{22} = 0.5$ and $\alpha_{12} = 0.17$.

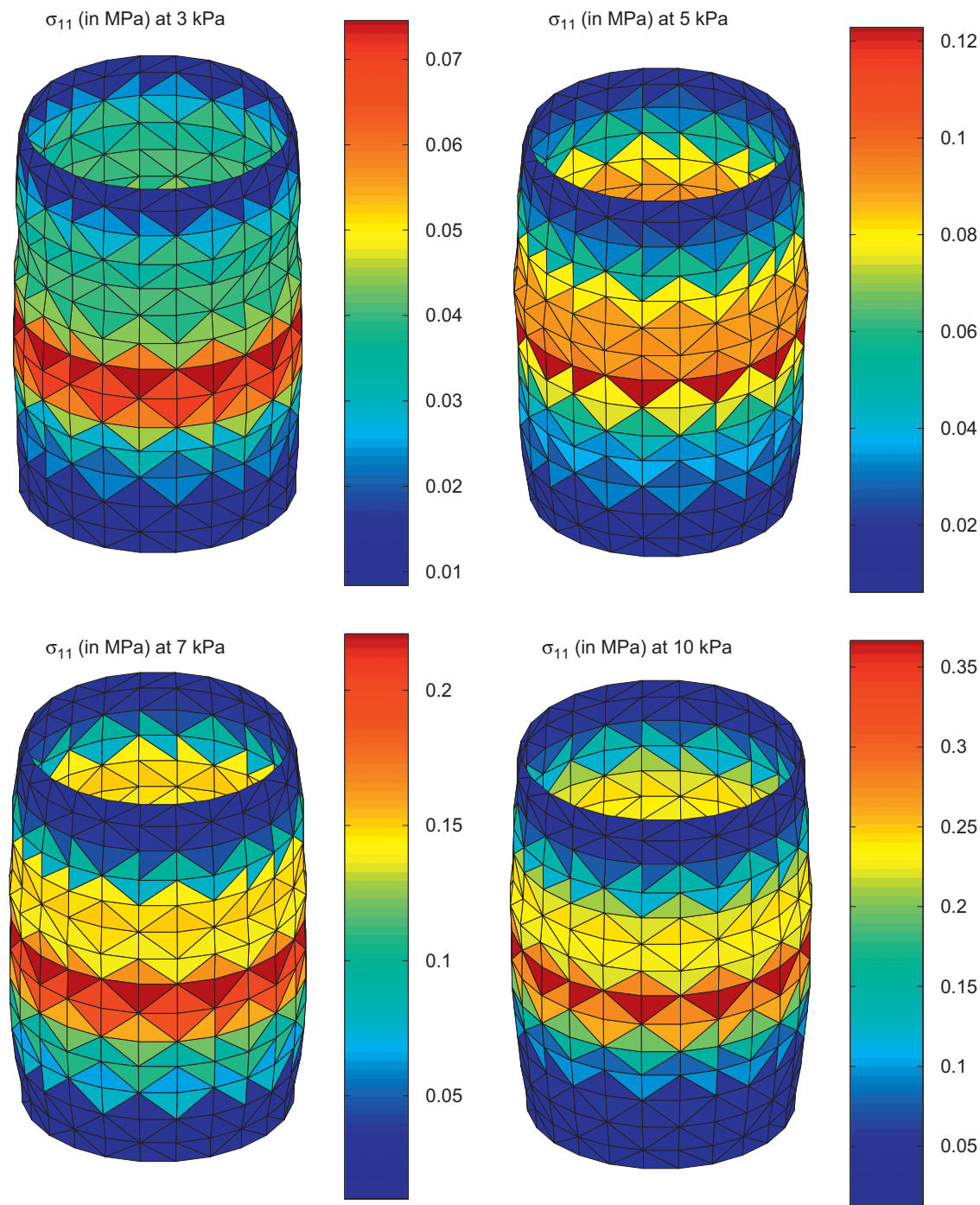


Fig. 4. Plot of the circumferential components of the Cauchy stress tensor for different values of p . The plot is displayed in the deformed configuration. The Cauchy stress is calculated with the Fung model using the identified values reported in Table 1.

Table 1
Results obtained with experimental data for the Fung model.

Parameter	β	α_{11}	α_{22}	α_{12}
Identified value	5 kPa	14.5	7	0.1

cost function to α_{12} , inducing the existence of a valley in the cost function.

The dependence of the VFM to the initializing values was not observed for the Holzapfel model.

Nevertheless, in the Holzapfel model, the exponential part is driven by only three material parameters, whereas the exponential part of the Fung model is driven by four material parameters. This supplementary material parameter in the Fung model does not affect sufficiently the value of cost function ζ in Eq. (10), inducing the lack of sensitivity to α_{12} . If one would like to increase the sensitivity to α_{12} , one would have to consider the response of the artery not only to incrementally varying pressures, but also to incrementally varying stretches in the axial direction, and to include these responses in the definition of cost function ζ . This will be considered in future studies.

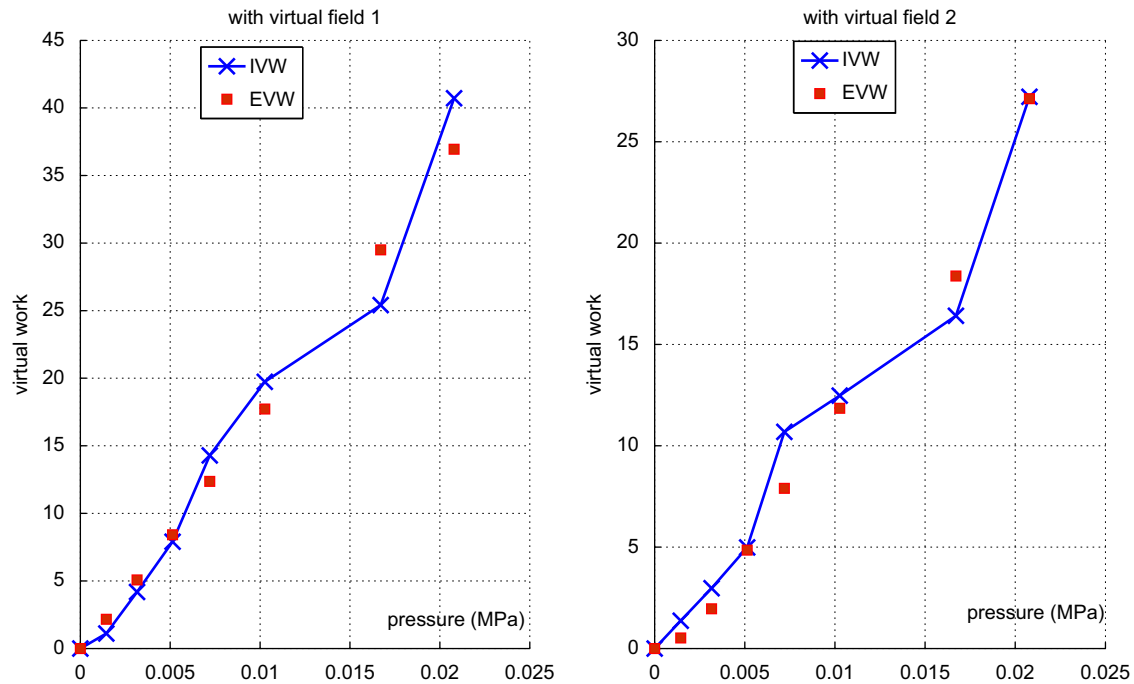


Fig. 5. Comparison of the internal and external virtual work for virtual field 1 (a) and virtual field 2 (b) when an anisotropic model is identified.

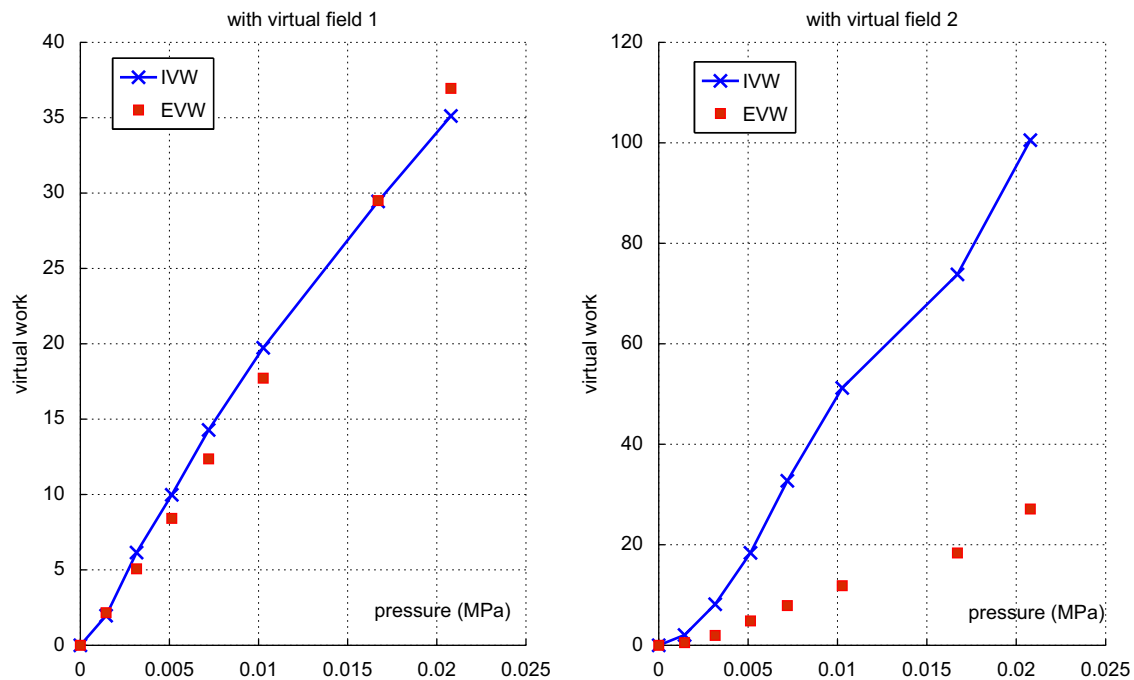


Fig. 6. Comparison of the internal and external virtual work for virtual field 1 (a) and virtual field 2 (b) when an isotropic model is identified.

4.3. Implementation of the identified model in a FE code

In Sun and Sacks (2005), the implementation of the Fung model in a FE code was discussed. In order to check the feasibility of utilizing this model with the parameters that we identified here (Table 1), computations were achieved on the geometry of the artery with the Abaqus[®] software. The geometry of the model is a 33.8 mm long cylinder with an initial diameter of 21.5 mm, and initial thickness of 1.3 mm. It was meshed with 1276 membrane elements (M3D4R type in Abaqus[®]). The Fung model

is a built-in feature of Abaqus[®], which requires the definition of a local coordinate system related to the anisotropy directions and the constitutive parameters reported in Table 1. No residual stress was incorporated in this model. One end of the cylinder was clamped. Regarding the other end, radial displacements were fixed and a longitudinal displacement was prescribed, corresponding to $L/L_0 = 1.1$. The different experimental pressure steps were applied successively. The resolution of the problem was performed using an implicit scheme accounting for large strains.

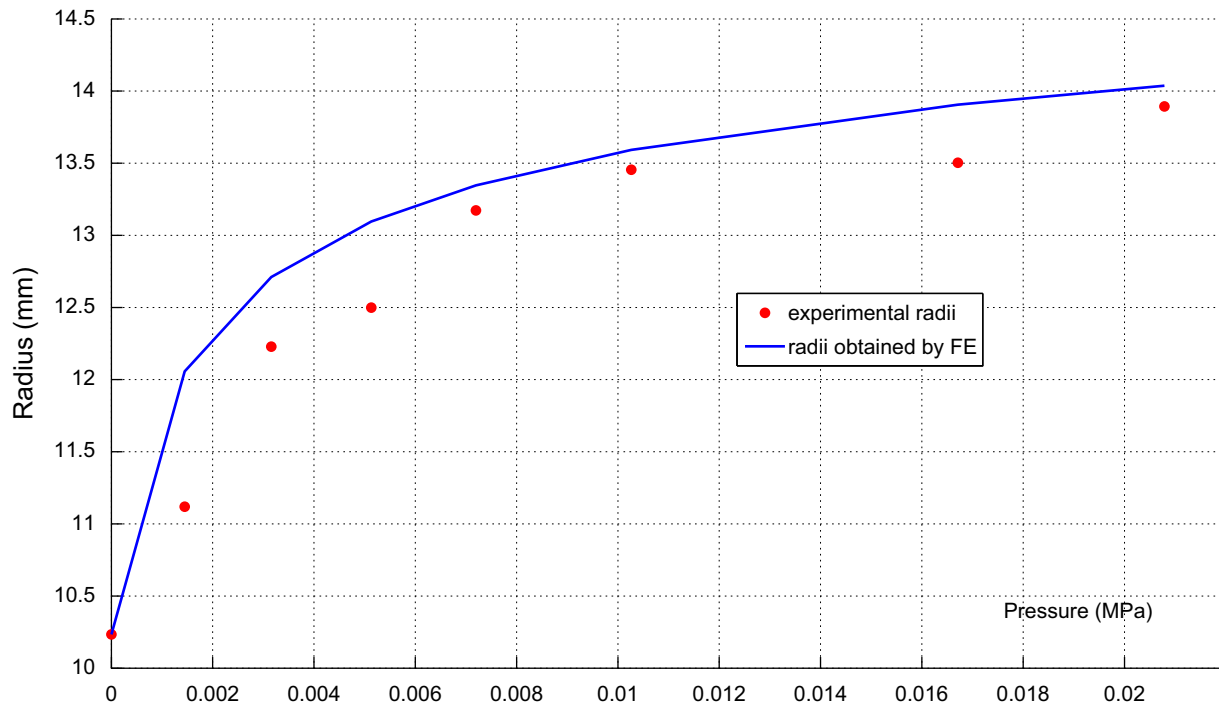


Fig. 7. Comparison of the deformed geometry between a FE model and experimental data.

A comparison of the average radii computed by Abaqus® to the measured average radii is shown in Fig. 7. The comparison is made for the cross section located at $z=(z_b+z_t)/2$, i.e. at midspan. The results show a good agreement.

However, the radii computed by FE model are slightly larger than the experimental ones. It may be induced by the fact that, in the model, we neglected the pressure applied by the physiological bath on the external surface of the artery (about 5 mmHg \approx 0.7 kPa at the midspan of the arterial segment). Discrepancies may also be induced by a difference between the experimental boundary conditions and the actual ones at the ends. For the FE model, the boundary conditions were of clamping type at both ends, whereas the actual ones are less rigid.

It is worth noting here that this discussion about the boundary conditions at both ends does not affect the results obtained by the VFM. Indeed, the effect of unknown reaction forces and parasitic motions at both ends is filtered out by the VFM. This is an essential asset of the VFM, as shown in Grédiac et al. (2006).

4.4. Derivation of average stress/strain curves

It was shown that the identified Fung model can be used to derive stress/strain curves of the artery, both in the circumferential direction and in the axial direction. Results are presented in the Appendices.

5. Conclusion

In conclusion, results presented in this work are promising regarding the application of the virtual fields method (VFM) for identifying the anisotropic hyperelastic properties of arteries. An innovative experimental device has been set up, calibrated and validated for characterizing arterial mechanical properties.

It is now important to carry out a large number of experiments for validating the approach with different sets of data and different tests. Other perspectives concern more complex loading conditions and more sophisticated models. More especially, next steps will

consist in (i) considering the possible heterogeneity of the properties and geometry of the artery wall, (ii) processing data from different loading cases (including torsion), (iii) and considering independently the different layers of arteries and the residual stresses. Achievement of these steps will require optimal spatial resolution and accuracy of the measurement technique, employing for instance 3-D digital image correlation (Sutton et al., 2007).

Conflict of interest statement

No conflict of interest.

Acknowledgements

The authors would like to thank Professeur Jean-Pierre Favre and to his staff in the Department of Cardiovascular Surgery at the University Hospital of Saint-Etienne (France), for their help in preparing the specimen tested in this study. The authors are also very grateful to Dr. Katia Genovese for the experimental work. This study is part of the Imandef Project (Grant ANR-08-JCJC-0071) funded by the ANR (French National Research Agency).

Appendix A. Supplementary data

Supplementary data associated with this article can be found in the online version at doi:10.1016/j.jbiomech.2010.07.004.

References

- Arimitsu, Y., Nishioka, K., Senda, T., 1995. A study of Saint-Venant's principle for composite materials by means of internal stress fields. *Journal of Applied Mechanics* 62, 53–62.
- Avril, S., Bonnet, M., Bretelle, A.-S., Grédiac, M., Hild, F., Ienny, P., Latourte, F., Lemosse, D., Pagano, S., Pagnacco, E., Pierron, F., 2008. Identification

- from measurements of mechanical fields. *Experimental Mechanics* 48 (5), 381–402.
- Avril, S., Grédiac, M., Pierron, F., 2004. Sensitivity of the virtual fields method to noisy data. *Computational Mechanics* 34 (6), 439–452.
- Avril, S., Huntley, J., Cusack, R., 2009. In-vivo measurements of blood viscosity and wall stiffness in the carotid using PC-MRI. *European Journal of Computational Mechanics* 18 (1), 9–20.
- Avril, S., Pierron, F., 2007. General framework for the identification of constitutive parameters from full-field measurements in linear elasticity. *International Journal of Solids and Structures* 44, 4978–5002.
- Einstein, D., Freed, A., Stander, N., Fata, B., Vesely, I., 2005. Inverse parameter fitting of biological tissues: a response surface approach. *Annals of Biomedical Engineering* 33 (12), 1819–1830.
- Foster, C., 1978. Measurement of radial deformations in thin-walled cylinders. *Experimental Mechanics* 18, 426–430.
- Fung, Y., 1993. *Biomechanics: Mechanical Properties of Living Tissues*. Springer, New York.
- Genovese, K., 2007. Radial metrology application to whole-body measurement on hyperelastic tubular samples. *Optics and Lasers in Engineering* 45 (11), 1059–1066.
- Genovese, K., 2009. A video-optical system for time-resolved whole-body measurement on vascular segments. *Optics and Lasers in Engineering* 47, 995–1008.
- Grédiac, M., Pierron, F., Avril, S., Toussaint, E., 2006. The virtual fields method for extracting constitutive parameters from full-field measurements: a review. *Strain* 42, 233–253.
- Hayashi, K., 1993. Experimental approaches on measuring the mechanical properties and constitutive laws of arterial walls. *ASME Journal of Biomechanical Engineering* 115, 481–488.
- Holzapfel, G., 2004. Experimental approaches on measuring the mechanical properties and constitutive laws of arterial walls. *Encyclopedia of Computational Mechanics. Solids and Structures* 2, 605–635.
- Holzapfel, G., Gasser, T., Ogden, R., 2000. A new constitutive framework for arterial wall mechanics and comparative study of material models. *Journal of Elasticity* 61, 1–48.
- Holzapfel, G., Sommer, G., Auer, M., Regitnig, P., Ogden, R., 2007. Layer-specific 3d residual deformations of human aortas with non-atherosclerotic intimal thickening. *Annals of Biomedical Engineering* 35 (4), 530–545.
- Humphrey, J., 1999. An evaluation of pseudoelastic descriptors used in arterial mechanics. *ASME Journal of Biomechanical Engineering* 121, 259–262.
- Humphrey, J., 2002. *Cardiovascular Solid Mechanics—Cells, Tissues and Organs*. Springer, New York.
- Marra, S., Kennedy, F., Kinkaid, J., Fillinger, M., 2006. Elastic and rupture properties of porcine aortic tissue measured using inflation testing. *Cardiovascular Engineering* 6, 125–133.
- Masson, I., Boutouyrie, P., Laurent, S., Humphrey, J., Zidi, M., 2008. Characterization of arterial wall mechanical behavior and stresses from human clinical data. *Journal of Biomechanics* 41 (12), 2618–2627.
- Matthys, D., Gilbert, J., Greguss, P., 1991. Endoscopic measurement using radial metrology with digital correlation. *Optical Engineering* 30 (19), 1400–1455.
- Nelder, J., Mead, R., 1965. A simplex method for function minimization. *Computer Journal* 7 (4), 308–313.
- Ogden, R., 1997. *Non-linear Elastic Deformations*. Dover Publication, New York.
- Promma, N., Raka, B., Grédiac, M., Toussaint, E., Cam, J.L., Balandraud, X., Hild, F., 2009. Application of the virtual fields method to mechanical characterization of elastomeric materials. *International Journal of Solids and Structures* 46, 698–715.
- Rastogi, P., 1999. *Photomechanics*. Springer Verlag.
- Seshaiyer, P., Humphrey, J., 2003. A sub-domain inverse finite element characterization of hyperelastic membranes including soft tissues. *Journal of Biomechanical Engineering* 125, 363–371.
- Slager, C., Wentzel, J., Schuurbijs, J., Oomen, J., Kloet, J., Krams, R., von Birgelen, C., van der Giessen, W., Serruys, P., de Feyter, P., 2000. True 3-dimensional reconstruction of coronary arteries in patients by fusion of angiography and IVUS and its quantitative validation. *Circulation* 102, 511–516.
- Sun, W., Sacks, M., 2005. Finite element implementation of a generalized Fung-elastic constitutive model for planar soft tissues. *Biomechanics and Modelling in Mechanobiology* 4, 190–199.
- Sutton, M., Ke, X., Lessner, S., Goldbach, M., Yost, M., Zhao, F., Schreier, H., 2007. Strain field measurements on mouse carotid arteries using microscopic three-dimensional digital image correlation. *Journal of Biomedical Materials Research Part A* 84A (1), 178–190.
- Sutton, M., Yan, J., Avril, S., Pierron, F., Adeeb, S., 2008. Identification of heterogeneous constitutive parameters in a welded specimen: uniform stress and virtual fields methods for material property estimation. *Experimental Mechanics* 48 (5), 451–464.
- Viotti, M., Albertazzi, A., Fantin, A., Pont, A.D., 2008. Comparison between a white-light interferometer and a tactile formtester for the measurement of long inner cylindrical surfaces. *Optics and Lasers in Engineering* 46, 396–403.